7

Lateral Surface Nanowires and Quantum Structures Based on ZnO

Hiroaki Matsui and Hitoshi Tabata
The University of Tokyo
Japan

1. Introduction

Zinc oxide (ZnO) has been important for the development of practical devices such as thin film transistors, magnetic semiconductors, transparent electrodes, and so on. ZnO has a large exciton energy of 60 meV, which raises the interesting possibility of utilizing excitonic effects at temperatures higher than 300 K (Thomas, 1960). Optically pumped UV stimulated emissions from ZnO layers have been demonstrated (Yu et al., 1997). Furthermore, $Mg_xZn_{1-x}O$ alloys are attracting a great deal of interest since they possess a higher band gap than ZnO (Sharma et al., 1999) and have been utilized for $Mg_xZn_{1-x}O$/ZnO multiple and single-quantum wells (Chen et al., 2000; Makino et al., 2000). These structures can form low-dimensional systems and produce interesting quantum phenomena such as an increased excitonic binding energy (Coli & Bajaj, 20001) and two-dimensional (2-D) electron transport aspects that contribute to both basic science and practical applications. (Tsukazaki et al., 2007).

A variety of nanostructures in semiconductor materials have been made and investigated. The number of papers concerning nanostructures in ZnO is increasing yearly. Self-organized techniques provide advantages for nanoscale engineering and have yielded many impressive results. Therefore, surface nanostructures in Si and GaAs have been fabricated using various growth mechanisms. Stranski-Krastanov (S-K) growth on lattice mismatched systems induces three-dimensional (3-D) nanodots on the 2-D wetting layers. Lateral surface nanowires have been fabricated by a step-faceting mode on vicinal surfaces (Schönher et al., 2001). These surface nanostructures have been developed for zero-dimensional (0-D) quantum dots and one-dimensional (1-D) quantum wires, respectively (Wang & Voliotis, 2006). Low-dimensional properties are currently receiving attention as advantages for optoelectronics with ZnO.

In epitaxial growth, lattice mismatch between an epilayer and a substrate plays a crucial role in epitaxy. Growth studies concerning ZnO epitaxy have been carried out using *c*- and *a*-sapphires (Vispute et al., 1997; Fons et al., 2000). Heteroepitaxial layers have a high dislocation density of 10^9 – 10^{10} cm^{-2} due to large mismatches in the lattice structure and thermal expansion (Viguè et al., 2001). The use of a ZnO substrate not only allows a reduction of the number of lattice defects involved in the epilayers, but also permits the selection of various growth directions without any lattice mismatch, which results in a direct understanding of growth dynamics. The growth polarity in ZnO is a primary factor. Zn (0001) and O (000-1) polarities have isotropic atom arrangements and possess spontaneous

Source: Nanowires, Book edited by: Paola Prete,
ISBN 978-953-7619-79-4, pp. 414, March 2010, INTECH, Croatia, downloaded from SCIYO.COM

polarization along growth directions. On the other hand, the *M*-nonpolar (10-10) surface has an anisotropic atom structure, and the spontaneous polarization occurs parallel to a surface plane (Parker et al., 1998). For example, Zn-polar growth produces atomically flat surfaces due to a layer-by-layer mode (Kato et al., 2003; Matsui et al., 2004), whereas *M*-nonpolar ZnO layers result in anisotropic morphologies with a nanowires structure based on a step-edge barrier effect (Matsui & Tabata, 2005). Thus, the difference in growth directions influences the surface state, as well as optical and electrical properties in ZnO layers, which are more conspicuous through quantum structures (Matsui & Tabata, 2008). Quantum structures on various surface morphologies exhibit novel electronic and optical properties because quantized energy levels can be tailored by varying the geometric dimensions.

This chapter is organized as follows. In Section 2, we first give a description of polar and nonpolar growth on ZnO layers and outline a difference of surface nanowires between ZnO and GaAs systems. The surface nanowires on the *M*-nonpolar ZnO (10-10) layer surface are largely different from those on high-index GaAs layer surfaces, indicating that the growth origin of surface nanowires on ZnO results from a new bottom-up process. In Section 3, we introduce layer growth using a pulse laser ablation technique. In Section 4, we discuss the growth origin of surface nanowires on ZnO layer surfaces from various viewpoints. Sections 4 and 5 are devoted to reports of anisotropic optical and electrical properties that are remarkably modulated by the anisotropic surface morphology. Some concluding remarks and future research directions in this field are given in Section 5.

2. Difference in surface nanowires of ZnO and GaAs

2.1 Polar and nonpolar ZnO layer surfaces

ZnO has a hexagonal wurtzite structure (a = 0.325 nm, c = 0.5201 nm) in which each Zn^{2+} ion bonds by a tetrahedron of four O^{2-} ions, representing a structure that can be described as a number of alternating planes of Zn and O ions stacked along the *c*-axis [Fig. 1a]. Various surface-sensitive methods have been well used to investigate the polar surfaces in ZnO from fundamental and applied points of view. For example, the surface morphology was quite different for opposite polar surfaces when ZnO crystals were chemically etched (Mariano & Hanneman, 1963). Thus, epitaxy in ZnO with varying polarity should show different

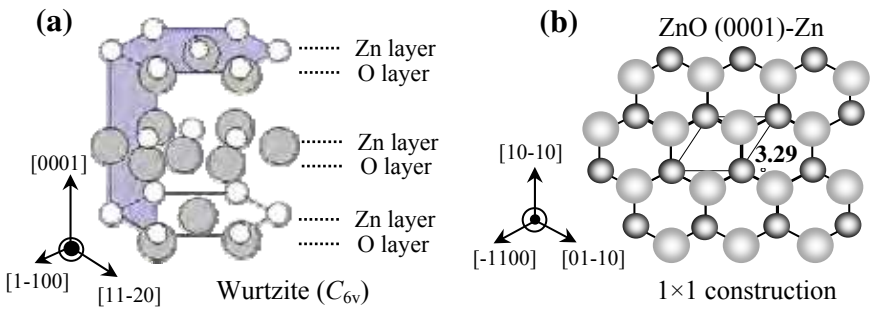

Fig. 1. (a) Schematic structure of ZnO with a stacking sequence of Zn and O layers. (b) Structural models showing the bulk-terminated Zn-polar (0001) surfaces of ZnO. The surface unit cells are indicated.

kinetics and material characteristics. Therefore, it is important to understand the uppermost surface structure and morphology in a Zn-polar surface. Figure 1(b) shows a structural model of the Zn-polar (0001) surfaces of ZnO. All O atoms on the borders have three nearest neighbours, i.e., only one bond is broken. The Zn-polar surface is unstable due to the existence of a non-zero dipole moment perpendicular to the surface, which raises a fundamental question regarding stabilization mechanisms.

Figure 2 shows the surface morphologies of Zn-polar, O-polar and *M*-nonpolar ZnO layers. The Zn-polar ZnO layer showed a very flat surface with a roughness of 0.21 nm [Fig. 2(a)]. The O-polar ZnO layer displayed a rough surface with a roughness of 4.2 nm and formed hexagonal islands [Fig. 2(b)]. The difference in surface morphology between Zn- and O-polar ZnO layers is similar to that for Ga- and N-polar GaN (0001) and Zn- and Se-polar ZnSe (111), which can be explained for in terms of the difference in the number of dangling bonds (Sumiya et al., 2000; Ohtake et al., 1998). In the case of Zn-polarity, the Zn atoms of ZnO molecules generated from the laser ablation are likely to be incorporated with less migration due to three dangling bonds. This suggests that Zn-polar growth should be dominated by a two-dimensional mode, resulting in very smooth surfaces. On the other hand, an O-polar surface has longer surface migration due to the single dangling bond and is adhered to the sites of the step edges with two dangling bonds. These result in hexagonal islands that originated from a spiral growth mode. The growth kinetics of O-polar growth has been suggested using molecular-dynamics crystal-growth simulations (Kubo et al., 2000).

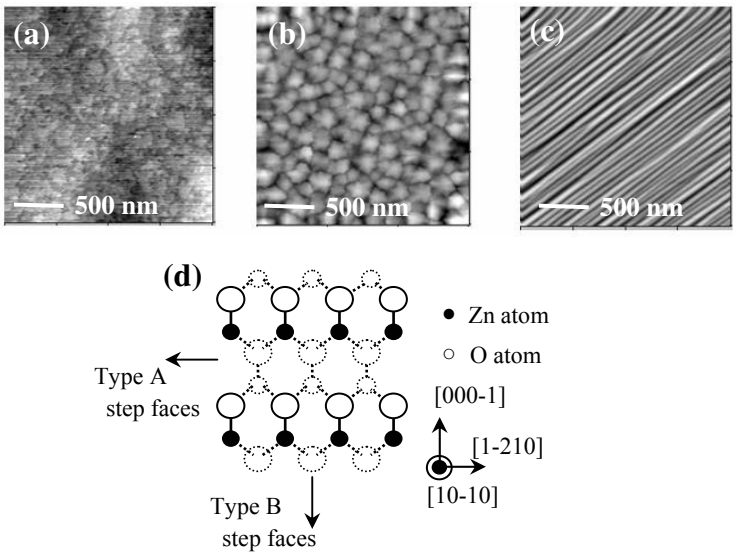

Fig. 2. AFM images of Zn-polar (a), O-polar (b) and *M*-nonpolar (c) ZnO layer surfaces. (d) Structural models showing the *M*-nonpolar (10-10) surfaces of ZnO.

On the other hand, the *M*-nonpolar ZnO layer surface showed a highly anisotropic surface morphology with self-organized surface nanowires elongated along the [0001] direction [Fig. 2(c)] (Matsui & Tabata, 2006). The stoichiometric ZnO (10-10) surface is auto-compensated since it contains an equal number of Zn and O ions per unit area. Zn and O atoms of the surface form dimer rows running along the [-12-10] direction, as shown in Fig.

2(d), which produces two types of A and B step edges consisting of stable low-index (-12-10) and (0001) planes, respectively (Dulub et al., 2002). The [-12-10] direction represents an auto-compensated nonpolar surface, while the [0001] direction consists of a polar surface with either Zn or O termination. This type of anisotropic surface structure has been utilized in scientific studies of heterogeneous catalytic processes involving the absorption of molecular and metallic atoms on nonpolar surfaces (Cassarin et al., 1999).

2.2 High-index GaAs layer surfaces

Similar surface nanostructures have been formed by a step-faceting growth mode on vicinal GaAs (775) *B* and (553) *B* substrates (Ohno et al., 2000; Yan et al., 2001). In GaAs, high-index or non-singular, planes are energetically unstable and tend to break up into low-index facets at normal epitaxial growth temperatures to minimize their surface energies. This process could produce periodic corrugations composed of nanometer-sized microscopic facets on originally flat surfaces. These ordered microscopic step arrays have been employed as the template for quantum wires. The most investigated high-index surfaces include (311) *A*, (331) *A* and (775) *B*. As an example, we present an AFM image of the GaAs (331) *A* layer surface in Fig. 3, which shows a highly anisotropic nanowire structure. The GaAs (331) *A* surface is thermally decomposed to a stable (111) *A* step and (110) terrace during homoepitaxial growth (Hong et al., 1988). This growth behaviour in GaAs indicates that the growth mechanism of the surface nanowires formed on non-vicinal ZnO (10-10) substrates differs from that of vicinal GaAs substrates. Thus, the surface nanowires on the low-index ZnO (10-10) surfaces are not fully related to the step-faceting process that was applied on the high-index GaAs surfaces.

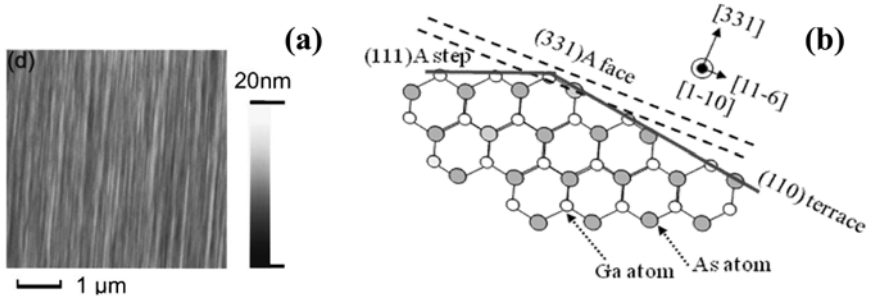

Fig. 3. (a) AFM image of the GaAs (331)*A* layer surface. (b) Schematic atom arrangement on cross-section with the [1-10] azimuth of the GaAs (331) *A* surface.

3. Experimental

ZnO layers and $Mg_{0.12}Zn_{0.88}O$/ZnO quantum wells (QWs) were grown at 400 - 600°C on *M*-plane ZnO (10-10) substrates (Crystec GmbH, Germany) using laser molecular beam epitaxy (laser-MBE). Figure 4 shows a schematic representation of the laser-MBE apparatus. The ZnO substrates were annealed *ex situ* at 1100°C in an oxygen atmosphere conducive to the formation of atomically flat surfaces, and then preannealed *in situ* at 600°C with an oxygen flow of 10^{-5} mbar for 20 min prior to laser-MBE growth. ArF excimer laser pulses (Compex 103: λ = 193 nm) were focused on ZnO and MgZnO targets located 4.5 cm from the substrates in an oxygen flow of 10^{-3} mbar. The number of Mg atoms in the MgZnO layer was

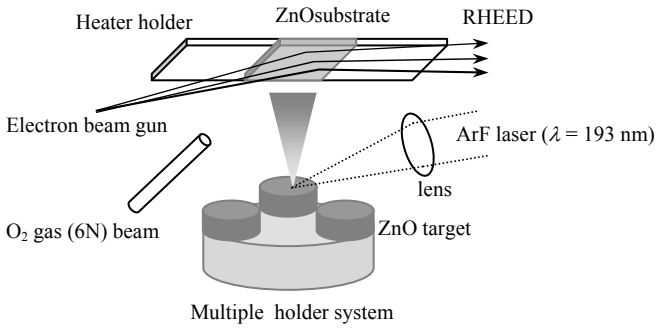

Fig. 4. A schematic figure of the laser-MBE apparatus.

estimated using an electron probe micro-analyzer (EPMA). The growth process was monitored using reflection high electron energy diffraction (RHEED).

Atomic force microscopy (AFM: Seiko SPI-3800) was used for observations of surface morphologies. Local structure analyses were conducted by means of high-resolution transmittance electron microscopy. Structural properties were characterized by high-resolution x-ray diffraction (HR-XRD: Philips X'pert) using a double-crystal monochromator. Micro-PL [(μ)-PL] spectroscopy was carried out at room temperature using a fourth harmonic generation of yttrium aluminium garnet laser (Nd^{3+}: YAG laser, 266 nm) excitation and a 0.85-m double monochromator (SPEX 1403) equipped with a nitrogen charge-coupled device camera. A reflective-type objective lens was used for this measurement to focus the laser to a diameter of 1 μm on the sample surface (Matsui et al., 2005). For polarized PL measurement, the sample was excited by a He-Cd laser (λ = 325 nm) in temperatures from 10 to 300 K. The luminescence was directed toward a Glan-Taylor prism to pick up polarization, and then passed through a depolarizer located behind the prism to eliminate the polarization. The spectrum was recorded using a 0.5-m single monochromator (SPEX 500M) equipped with a 1200 grooves/cm grating blazed at 500 nm. Electrical properties were measured using a four-probe Hall bar configuration with the perpendicular arms of the Hall bar aligned carefully in the [0001] and [11-20] directions. The Hall bars were fabricated by Ar ion milling of the samples through a photolithography-defined resist mask. The *ex situ* annealed ZnO substrate was treated as a semi-insulating substrate showing electrical resistivity in the order of 10^6 – 10^7 Ω cm.

3. Origin of surface nanowires

3.1 Growth evolution and structural quality

We describe the growth process and morphological evolution of the surface nanowires on the basis of RHEED and AFM investigations. The ZnO layers were grown at 550°C. At the very beginning of layer growth up to 8 nm in thickness, a 2D streak pattern appeared in place of sharp patterns of the ZnO substrates [Fig. 5(a) and 5(b)]. This is related to 2D nucleation at the initial growth stage, as evidenced by the smooth layer surface [Fig. 5(f)]. Continued growth of ZnO changed to a mixed pattern, which relates to the onset of the transition from 2D to 3D modes. This resulted from the appearance of a self-assembly of

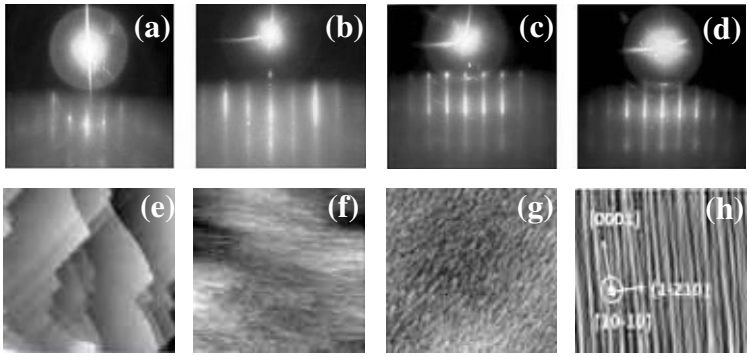

Fig. 5. RHEED patterns with the [0001] azimuth of the treated ZnO substrate (a) and ZnO layers with a thickness of (b) 8, (c) 20 and (d) 240 nm. AFM top view (2 x 2 μm²) of the treated ZnO substrate (e) and ZnO layers with different thicknesses [(f)-(h)]. Layer thicknesses are (f) 8, (g) 20 and (h) 250 nm

anisotropic 3D islands [Fig. 5(c) and 5(g)]. Finally, the RHEED pattern showed 3D spots due to an island growth mode that originated from the formation of surface nanowires [Fig. 5(d) and 5(h)]. Surface nanowires with high density (10^5 cm^{-1}) that formed on the ZnO layers were homogeneously elongated along the [0001] direction above 5 μm with a few branches. Due to lattice strains at the heterointerface of a layer/substrate, S-K growth naturally induces 3D islands that are surrounded by high-index facets on 2D wetting layers. This has been observed in InGaAs/GaAs heteroepitaxy (Guha et al., 1990; Matsui et al., 2006). In an effort to examine the crystallinity in greater detail, plan-view and X-TEM observations were conducted to investigate the structural quality of the layer. Figure 6 (a) shows a low-

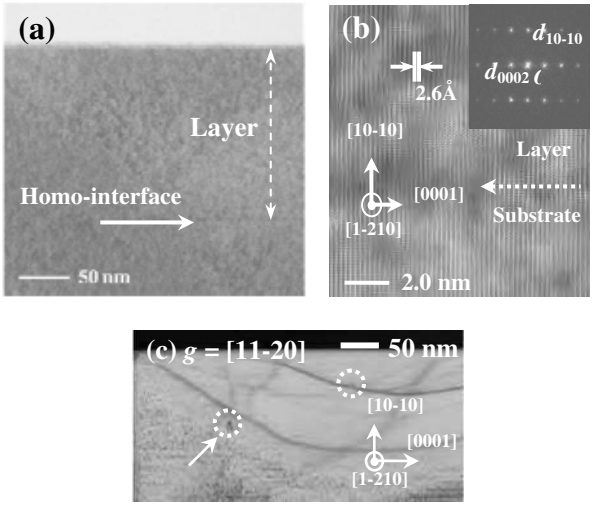

Fig. 6. (a) Low- and high-resolution X-TEM images of the ZnO layer taken with the [11-20] zone axis. Inset shows the RSD obtained by FFT analysis. (c) A bright field plan-view TEM image of the ZnO layer with *g* = [11-20] excitation under two-beam conditions.

resolution X-TEM image with the [11-20] zone axis. Threading dislocations induced by lattice relaxation between the layer and substrate were not observed. The high-resolution X-TEM image in Fig. 6(b) reveals a lattice arrangement between a smoothly connected layer and substrate. A 3 x 3 nm^2 space area selected from the layer region was utilized for a fast Fourier transform (FFT) analysis to examine local lattice parameters, and yielded a reciprocal space diffractogram (RSD) pattern [inset of Fig. 3(b)]. From the RSD pattern, the estimated strains (ε_{yy} and ε_{zz}) at the interface were approximately 0.10% and 0.18% with x, y and z being parallel to the [0001], [10-10] and [11-20] directions, respectively. Figure 6(c) shows a bright field plan-view TEM image with g = [11-20] excitation under two-beam conditions. Out-of-plane dislocations, marked by white open circles, were observed with a density of 3.2 x 10^7 cm^{-2}, and originated from threading dislocations running perpendicular to the layer surface. On the other hand, there were no in-plane dislocations propagated along the [0002] and [11-20] directions for different g vector excitations. These results indicate that the homoepitaxial interface was almost strain free. Thus, the elongated 3D islands that appeared on the 2D layers were formed under coherent homoepitaxy and had no correlation with S-K growth.

3.2 Characteristics of surface nanowires

Figure 7(a) and 7(b) show low-and high-resolution X-TEM images with the [0001] zone axis, respectively. A cross section of the surface nanowires displayed a triangular configuration with a periodicity of 84 nm. A high-resolution X-TEM image, marked by a white circle, revealed that the side facets did not consist of high-index facets, but instead had a step-like structure with a height of 0.27 nm that corresponded to half a unit of the *m*- axis. Side facets of the surface nanowires possessed uniform step spacing ranging from 0.1 to 0.2 nm, and were not surrouded by the high-index facets. A large number of surface nanowires showed flat tops with a (10-10) face and were separated laterally by deep grooves, as illustrated schematically in Fig. 7(e). A similar structure was also seen in the anisotropic 3D islands on the 20 nm-thick layers, which indicated that the surface nanowires resulted from a coarsening of anisotropic 3-D islands formed at the initial growth stage.

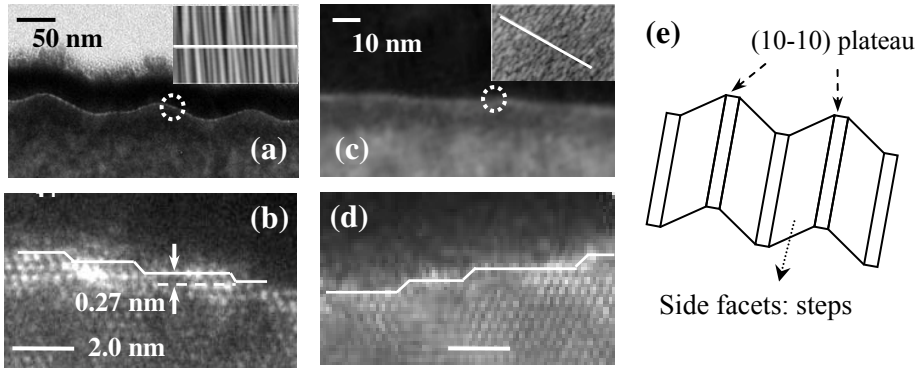

Fig. 7. (a) Low-and (b) high-resolution X-TEM images of the ZnO layer with a thickness of 240 nm. (c) Low-and (d) high-resolution X-TEM images of a 20 nm-thick ZnO layer. Insets (a) and (c) represent AFM images of the ZnO layers used for X-TEM observations. (e) Schematic representation of surface nanowires identified from X-TEM images.

The dependence of lateral periodicity of arrays on the thickness of the ZnO layers at a growth temperature (T_g) of 420°C was initially investigated, as shown in Fig. 8(a). The ZnO layers with layer thickness below 10 nm possessed flat surfaces. With increasing a layer thickness up to 15 nm, anisotropically small islands formed along the [0001] direction formed on the layer surface, and then developed to the surface nanowires. The lateral periodicity was 28 nm for the 15 nm-thick ZnO layer, and was almost saturated at 43 nm for ZnO layers with a thickness between 50 and 380 nm. The critical layer thickness, which completely developed to the surface nanowires, was approximately 0.1 μm. The dependence of the saturated lateral periodicity on growth temperature was also investigated. The lateral periodicity increased monotonically from 42 nm at T_g = 420°C to T_g = 600°C [Fig. 8(b)].
The saturation of the lateral periodicity with the layer thickness suggested that the surface migration of Zn-related ablation species, such as ZnO and Zn, supplied from the ablation targets is limited by the terrace width of the side facets (Ohtomo, et al., 1998). This was in agreement with the notion that the increase in periodicity with increasing growth temperature was due to prolonged surface diffusion of ablated species at high temperatures. The importance of surface diffusion was demonstrated using $Mg_xZn_{1-x}O$ alloys. An inhomogeneity in nanowire length with increasing Mg content was found in surface nanowires on layer surfaces of $Mg_xZn_{1-x}O$ (10-10) layers, although the lateral periodicity remained unchanged [Figs. 8(c) and 8(d)]. This may have been due to differences in surface migration and sticking probabilities of Zn- and Mg-related species. Thus, surface diffusion plays an important role in determining the size of nanowires, depending on the growth conditions and surface compositions. Moreover, highly anisotropic morphologies must be related because surface diffusion is much faster along the [0001] direction.

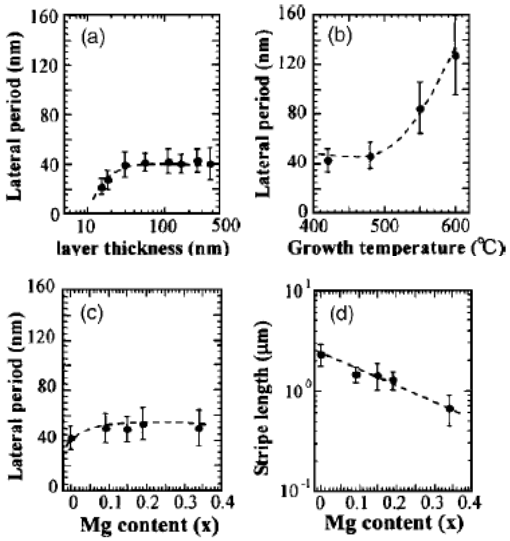

Fig. 8. (a) Dependence of lateral periodicity on layer thickness of ZnO layers at T_g = 420°C. (b) Dependence of saturated lateral periodicity on growth temperature of ZnO layers. (c) Dependence of lateral periodicity on Mg content of $Mg_xZn_{1-x}O$ layers at T_g = 420°C. (d) Dependence of nanowire length on Mg content (x) of $Mg_xZn_{1-x}O$ layers at T_g = 420°C.

3.3 Growth mechanism of surface nanowires

A multilayer morphology is determined not only by the transport of atoms within an atom layer (*intralayer transport*), but also by the transport of atoms between different atomic layers (*interlayer transport*). Thus, evolution of mound shapes is understood in terms of activation of atomic processes along the step edge. Therefore, a sequence of multilayer growth is governed by activation of atomic processes which enable exchange and hopping of atoms between different layers [Fig. 9(a)]. Schwoebel and Shipsey introduced the schematic potential energy landscape near a step that become the signature of what is often referred to as the Ehrlich-Schwoebel barrier (ESB) with a barrier energy of ΔE (Schwoebel, 1966). The mass transport of atoms between different layers is inhibited by a strong ESB effect, resulting in mound formation. This induces a nucleation of islands on the original surface together with inhibited interlayer transport. Once the islands are formed, atoms arriving on top of the islands will form second layer nuclei, and on top of this layer, a third layer will nucleate. This repetition leads to an increase in surface roughness with increasing layer thickness (Θ), resulting in the formation of mound shapes.

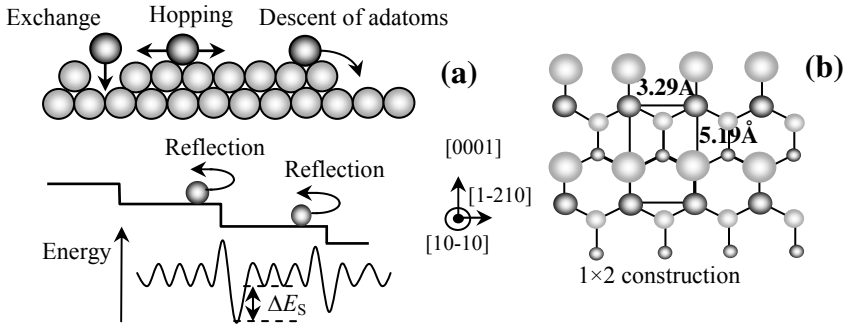

Fig. 9. (a) Upper part of the figure shows the descent of adatoms from an island by hopping and exchange. The lower part illustrates the energy landscape for hopping and the definition of ΔEs. (b) Structural models showing the M-nonpolar (10-10) surfaces of ZnO. The surface unit cells are indicated.

Mound formation is often observed on various systems such as semiconductors, metals, and organic materials. A mound structure possesses a small flat plateau at the top and a side facet with constant step spacing, and is separated from other mounds by deep grooves. This structure has been observed on dislocation-free metal homoepitaxial surfaces such as Pt/Pt (111) and Ag/Ag (100) systems, and is often referred to as a wedding cake (Michely & Krug, 2004). Here, mound formation emerging under reduced interlayer transport is described using the coarsening $\lambda \sim \Theta^n$, and the surface width $w \sim \Theta^\beta$. λ and w values are the height-height correlation between the nanowires and the surface roughening, respectively. As seen in Figs. 10(a) and 10(b), a coarsening exponent was indicated by $n = 0.23$, which was close to the n value of mound formation appearing during homoepitaxy. Moreover, the high β value of 0.60 was suitable for mound growth based on the ESB. This indicates that the surface nanowires formed during *M*-nonpolar ZnO homoepitaxy are due to the growth process originating at the ESB (Yu & Liu, 2008). The ESB was also seen for layer growth of O-polar ZnO with a hexagonal island surface. The appearance of an anisotropic morphology is related closely to a difference in surface diffusion and sticking probability as an important parameter. In *M*-nonpolar ZnO, the stoichiometric surface is auto-compensated since it

contains an equal number of Zn and O ions per unit area. Surface Zn and O atoms form dimer rows running along the [1-210] direction, as shown in Fig. 6(b). This produces two types of A and B step edges consisting of stable low-index (1-210) and (0001) planes, respectively. The [1-210] direction represents an auto-compensated nonpolar surface, while the [0001] direction consists of a polar surface with either Zn or O termination. Thus, the origin of the surface nanowires is based not only on an ESB effect, but a difference in surface diffusion and sticking coefficient of atoms between the two types of step edges.

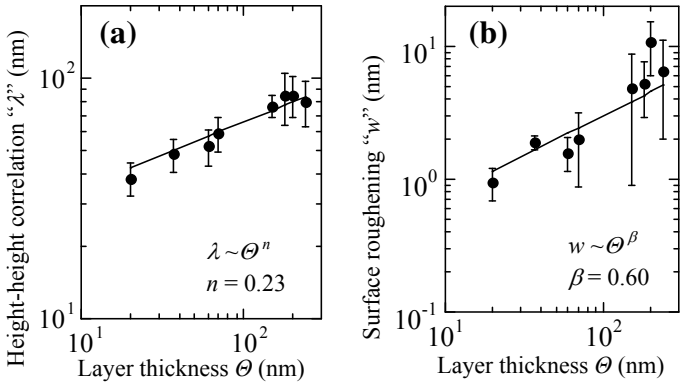

Fig. 10. (a) Height-height correlation (λ) and surface roughening (w) as a function of layer thickness.

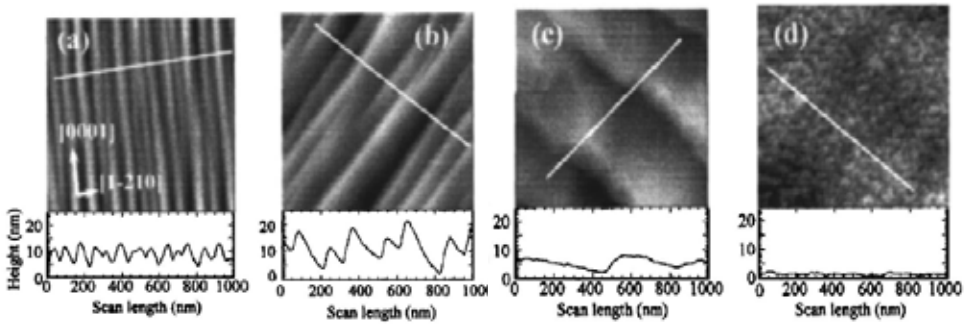

Fig. 11. AFM images (1 μm x 1μm) and cross-section profiles of ZnO layers on vicinal ZnO (10-10) substrates with off-angle of 0°-, 5°-, 10°-, and 15° from the (10-10)-oriented surface toward the (21-10)-oriented surface, indicated by (a), (b), (c), and (d), respectively. All nanowire arrays were elongated along the [0001] direction.

Anisotropic island growth on GaAs (001) based on the ESB effect is suppressed using vicinal GaAs (001) substrates with an off angle above a certain value (Johnson et al., 1994). AFM images of the ZnO layers on the vicinal substrates are shown in Fig. 11. With an increasing off angle, the cross-section profile of the AFM images gradually changed from symmetric to asymmetric shapes following the increase in lateral periodicity. The ZnO layer yielded a smooth surface with a roughness below 2 nm when the off angle of the substrate reached 15°. The off angle of 15° was close to that of the inclination of the surface nanowires. Figures 10 and 11 indicate that the surface nanowires originated from the ESB mechanism.

4. Band gap engineering and quantum wells (QWs)

4.1 $Mg_xZn_{1-x}O$ alloys

The discovery of tenability of a band gap energy based on ZnO has made the alloy system a promising material for use in the development of optoelectronic devices. Characterization of alloys such as (Mg,Zn)O or (Cd,Zn)O is important from the viewpoint of band gap engineering and the *p-n* junction. It was found that a $Mg_xZn_{1-x}O$ alloy was a suitable material for the barrier layers of ZnO/(Mg, Zn)O super-lattices due to its wider band gap. Since the ionic radius of Mg (0.56Å) is very close to that of Zn^{2+} (0.60Å), Mg-rich (Mg, Zn)O alloys with a wurtzite phase have been stably converted even when a rock salt-structured MgO is alloyed. A Mg content doped into a ZnO layer usually depends on the surface polarity, a growth technique, and type of substrate. Figure 12(a) shows the Mg content in $Mg_xZn_{1-x}O$ layers as a function of the target Mg content. Under growth conditions in this work, the Mg content in Zn-polar layers was always 1.6 times higher than the content in the ablation targets. This can be attributed to the low vapor pressure of Mg-related species compared to that of Zn. The incorporation efficiency of Mg atoms into the layers is more enhanced for O-polarity. On the other hand, the incorporation efficiency of Mg atoms in the case of a *M*-nonpolar surface is located between Zn- and O-polarities because the *M*-nonpolar surface has two dangling bonds, while Zn- and O-polarities have three and one-dangling bond, respectively. With increasing Mg content, the band gap systematically increased at 300 K as shown by the results of reflectance spectroscopy [Fig. 12(b)].

4.2 MgZnO/ZnO superlattices

A micro (μ)-PL technique is a powerful technique and can be employed to examine phase separation problems in MgZnO alloy layers. Figure 13(a) shows the variation in non-polarized μ-PL spectra at room temperature for $Mg_xZn_{1-x}O$ layers (x = 0 – 0.34). Band-edge emissions of all layers were systematically shifted to high energies with the Mg content alloys with different Mg contents at micro-scale. A driving force for the phase separation is closely related to lattice relaxation based on observations of Zn- and O-polar $Mg_xZn_{1-x}O$ homoepitaxial layers (Matsui et al., 2006). Therefore, a single phase of *M*-nonpolar $Mg_xZn_{1-x}O$ layers is only obtained below x = 0.12. 7-period $Mg_{0.12}Zn_{0.88}O$/ZnO MQWs were grown

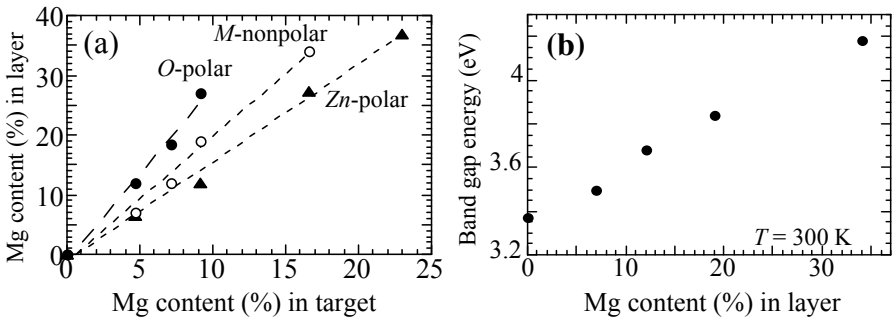

Fig. 12. (a) Mg contents in Zn-polar, O-polar and *M*-nonpolar $Mg_xZn_{1-x}O$ layers as a function of the target contents. (b) Dependence of band gap energy on Mg content for M-nonpolar $Mg_xZn_{1-x}O$ layers.

on ZnO layers with surface nanowires at T_g = 550°C and $p(O_2)$ = 10^{-3} mbar. The barrier thickness was set to 7 nm, and the well width was controlled from 1.4 to 4 nm. Figure 13(b) shows an AFM image of MQWs with a L_W of 2.8 nm. Surface nanowires elongated along the [0001] direction were homogeneously retained even after growing the MQWs. Figure 9(c) shows an X-TEM image of MQWs with the [0001] zone axis. The layer with a bright contrast represents MgZnO barriers, while the dark layers represent ZnO wells, which indicate that the MgZnO layers repeat the surface structure of the underlying ZnO layers.

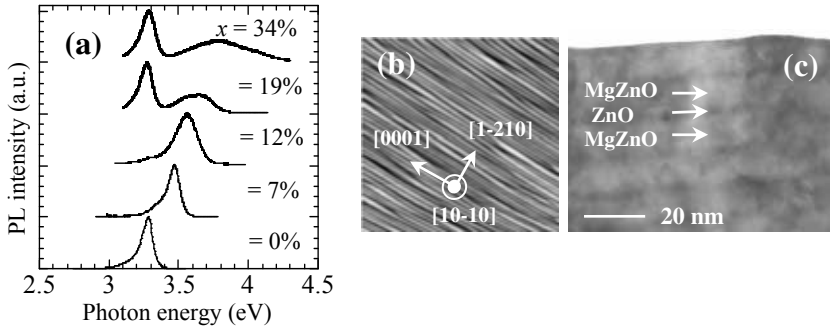

Fig. 13. (a) Non-polarized μ-PL spectra of $Mg_xZn_{1-x}O$ layers (x = 0, 0.07, 0.12, 0.19 and 0.34). The emission peak at 3.2 eV originates from the ZnO substrates. (b) Surface morphology and (c) X-TEM image of $Mg_{0.12}Zn_{0.88}O$/ZnO QWs with a L_W = 2.8 nm.

5. Anisotropic optical properties of MQWs

5.1 Linear polarized emissions

ZnO has attracted great interest for new fields of optical applications. Interesting characteristics of wurzite structure include the presence of polarization-induced electric fields along the c-axis. However, the optical quality of a quantum-well structure grown along the c-axis suffers from undesirable spontaneous and piezoelectric polarizations in well layers, which lower quantum efficiency. The use of nonpolar ZnO avoids this problem due to an equal number of cations and anions in the layer surface. Nonpolar ZnO surfaces have in-plane anisotropy of structural, optical, acoustic, and electric properties, which is useful for novel device applications. In this session, we discuss polarized PL of *M*-nonpolar ZnO layers and $Mg_{0.12}Zn_{0.88}O$/ZnO QWs.

Figure 14 shows splitting of the valence band (VB) in ZnO under the influence of crystal-field splitting and spin-orbit coupling. The VB of ZnO is composed of *p*-like orbitals. Spin-orbit coupling leads to a partial lifting of the VB degeneracy, and the former six-fold degenerate VB is split into a four-fold (j = 3/2) and two-fold (j = 1/2) band. The spin-orbit coupling is negative. The j = 1/2 band is at a higher energy than the j = 3/2 band. On the other hand, the crystal field in ZnO results in further lifting of the VB degeneracy due to the lower symmetry of wurtzite compared to zinc blende. The crystal field causes a splitting of *p* states into Γ_5 and Γ_1 states. Crystal-field splitting Δ_{cf} and spin-orbit coupling Δ_{so} together give rise to three types of two-fold degenerate valence bands, which are denoted as A (Γ_9-symmetry), B (Γ_7) and C (Γ_7) (Reynolds et al., 1999). These energies are formulated as follows:

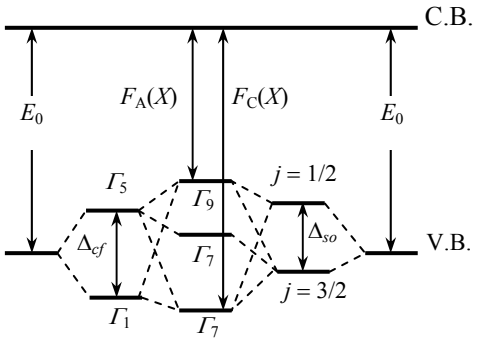

Fig. 14. Schematic energy level of band splitting by the crystal-field (Δ_{cf}) and spin-orbit (Δ_{so}) interactions in a wurtzite structure. $F_A(X)$ and $F_C(X)$ correspond to *A* and *C*-excitons, respectively, which are indicated in the middle. In the electronic energy levels proposed by Park *et al.* and Reynolds *et al.*, the uppermost Γ_9 and Γ_7 levels are interchanged.

$$E_A(\Gamma 9) - E_B(\Gamma 7) = -\frac{\Delta SO + \Delta cf}{2} + \frac{\sqrt{(\Delta SO + \Delta cf)^2 - \frac{8}{3}\Delta SO\Delta cf}}{2} \quad (1)$$

$$E_A(\Gamma 9) - E_C(\Gamma 7) = \sqrt{(\Delta SO + \Delta cf)^2 - \frac{8}{3}\Delta SO\Delta cf} \quad (2)$$

For ZnO, the experiment gave E_A-E_B = 0.0024 eV and E_C = 0.0404 eV (Fan et al., 2006). Solving the above two equations, we obtain Δ_{cf} (0.0391 eV) and Δ_{so} (-0.0035 eV). *A*- and *B*-excitons are referred to as heavy (HH) and light hole (LH) bands, respectively, and the crystal-field split-off hole (CH) was related to the *C*-exciton. The detection of $E \perp c$ and $E // c$ points to *A*-exciton (X_A) and C-exciton (X_c), respectively, where *E* represents the electric field vector (Reynolds et al., 1999).

Figure 15(a) shows the $E \perp c$ and $E // c$ components of the normalized PL spectra of strain-free ZnO layers (Matsui &Tabata, 2009). Polarization direction is referenced in Fig. 16 (a). The peak energies of X_A and X_C were located at 3.377 and 3.419 eV, respectively. These energies coincided with the X_A (3.377 eV) and X_C (3.4215 eV) peaks in ZnO crystals, respectively. The dependence of peak intensities on temperature could be fitted using the Bose-Einstein relation with a characteristic temperature of 315 and 324 K from the X_A and X_C peaks, respectively. The bound exciton (D^0X) peak disappeared at 120 K due to the activation energy of 16 meV. The polarization degree (*P*) is defined as $(I_\perp - I_{//}) / (I_\perp + I_{//})$, where $I_\perp$ and $I_{//}$ are the peak intensities for $E \perp c$ and $E // c$, respectively. Figure 15 (b) shows the polarization-dependent PL spectra at 300 K. The layer strongly emitted polarized light. The *P* value was calculated as 0.49. Significant spectral shifts in PL were detected when altering the polarization angle. This is attributed to a difference in carrier distribution in the VB between the HH and CH levels at 300 K. Figure 15(c) shows the dependence of polarization angle on PL intensity. Experimental data (triangle dots) were in agreement with the $\cos(\theta)^2$ fit line (solid) obeyed by Malus' law.

5.2 In-plane anisotropy of MQW emissions

The polarization PL character in *M*-nonpolar MQWs is now discussed. ZnO wells are strain-free in the case of pseudomorphically grown MgZnO/ZnO MQWs. The PL spectra for $E \perp c$ and $E//c$ in MQWs with a well thickness (L_W) of 2.8 nm are shown in Fig. 16(a).

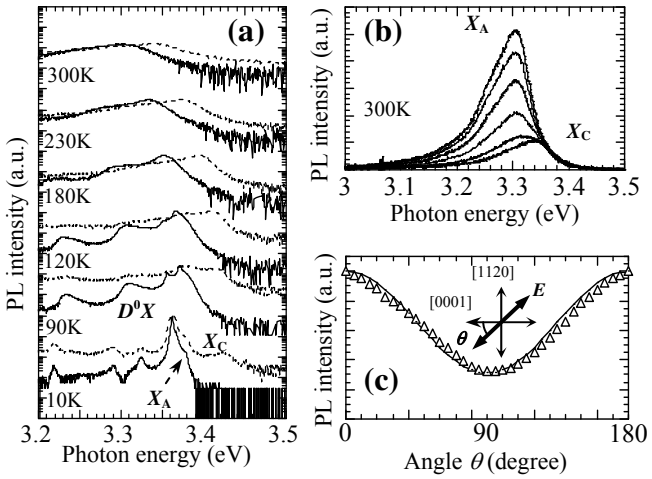

Fig. 15. (a) Temperature dependence of PL spectra on strain-free ZnO layers for $E \perp c$ (solid lines) and $E//c$ (dotted lines). (b) Polarization-dependent PL spectra at 300 K taken in steps of $\Delta\theta = 15^{o}$. (c) PL intensity as a function of polarization angle θ. Inset shows a schematic representation of the measurement geometry and sample orientation

The emission peaks around 3.6 eV correspond to 7 nm-thick $Mg_{0.12}Zn_{0.88}O$ barriers. At 300 K, an energy separation (ΔE) of 37 meV was found between the MQWs emissions of 3.372 eV ($E \perp c$) and 3.409 eV ($E//c$). The emission peak for $E \perp c$ appeared under conditions of $E//c$ below 120 K since the thermal distribution of carriers in the high-energy level for $E//c$ is negligible at 10 K. A polarization degree close to unity was found with a high P of 0.92 at 10 K [Fig. 16(c)]. In contrast, excited carriers at 300 K were sufficiently distributed in the high-energy level, resulting in a low *P* of 0.43. Furthermore, ΔE between the emission peaks for $E \perp c$ and $E//c$ was retained at around 40 meV even at 60 K [Fig. 16(d)]. This ΔE was close to the theoretical ΔE between the X_A and X_C states (Mang et al., 1999). For unstrained bulk ZnO, a polarization magnitude of zero and unity in the *C*-exciton is detected along the normal direction and along the *c*-axis, respectively [Fig. 15(a)]. However, the confinement of *M*-nonpolar MQWs takes place perpendicular to the quantization of the [10-10] direction. This result generates weak mutual mixing of the different *p* orbitals. Therefore, a π polarization component is expected for the A-excitonic state in these MQWs. In the case of *M*-nonpolar MQWs, it is predicted that a 10% p_z orbital component is involved with the *A*-excitonic states (Niwa et al., 1996), which is in agreement with the experimentally obtained *P* value of 0.92. MQWs with a L_W of 1.4 nm showed that the polarized PL spectra of $E \perp c$ and $E//c$ were separated by a small ΔE of 27 meV at 300 K [Fig. 16(b)]. ΔE decreased with temperature, and then completely disappeared at 60 K. The *P* value also dropped for all of the temperature regions. These behaviours are due to a large admixture of p_x to p_z orbitals

for E//c, originating from an inhomogeneous roughening between the well and barrier layers. The interface roughness increased a potential fluctuation of quantized levels in the MQWs, being reflected by the broadened PL lines (Waag et al., 1991).

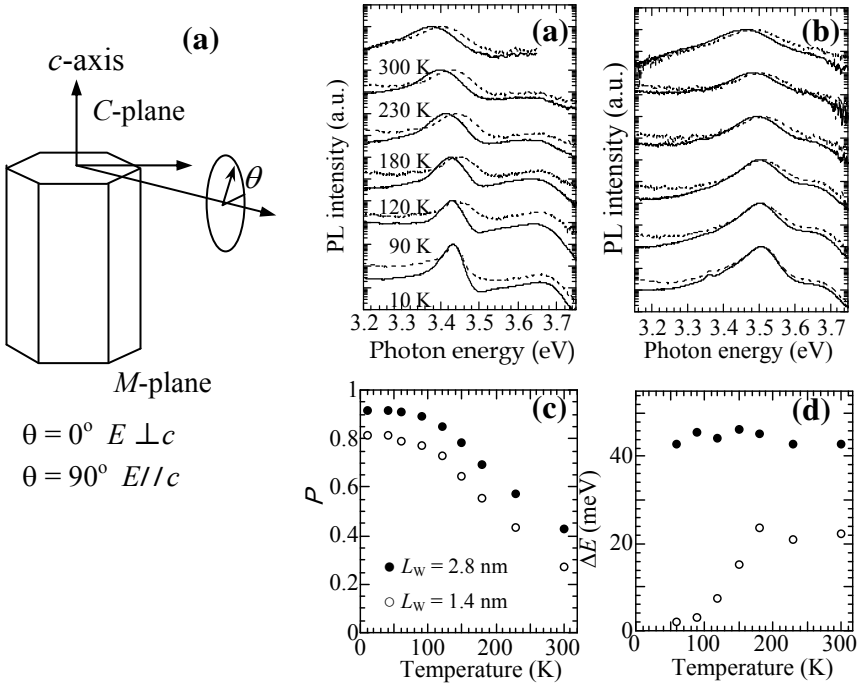

Fig. 16. PL spectra under $E \perp c$ (solid lines) and $E//c$ (dotted lines) on MQWs with L_W = 2.8 nm (a) and 1.4 nm (b). (c) and (d) show the relationship of temperature with polarization degree (P) and energy separation (ΔE) on MQWs with different L_W.

6. In-pane anisotropy of conductivity on MQWs for quantum wires

Transport properties were determined using a double Hall bar configuration with the [0001] and [1-210] directions [Fig. 17(a) and 17(b)]. Figure 17 (b) shows the temperature-dependent Hall mobility parallel ($\mu_{H[0001]}$) and perpendicular ($\mu_{H[1\text{-}210]}$) to the nanowires. $\mu_{H[0001]}$ gradually increased with decreasing temperature and was almost retained below 150 K due to a suppression of ionized impurity scattering. The electron concentration of MQWs also saturated below 70 K, suggesting that the whole electric current flows as 2D-like transport through the ZnO wells. On the other hand, $\mu_{H[1\text{-}210]}$ was much lower and resulted in large anisotropy of electron transport. The nature of the large transport anisotropy was evaluated by examining the temperature dependence of the conductivity (σ) for both directions [Fig. 17 (c)]. $\sigma_{[0001]}$ parallel to the nanowire arrays was almost independent of temperature below 70 K. Furthermore, the carrier concentration (n_e) was also constant below 70 K, suggesting that $\sigma_{[0001]}$ possessed metallic conductivity. In contrast, $\sigma_{[1\text{-}210]}$ perpendicular to the nanowire increased exponentially with T^{-1} in the region from 70 to 10 K. The activation energy E_a was

12 meV, indicating that an effective potential barrier height of 12 meV is formed for electron motion perpendicular to the nanowire arrays.

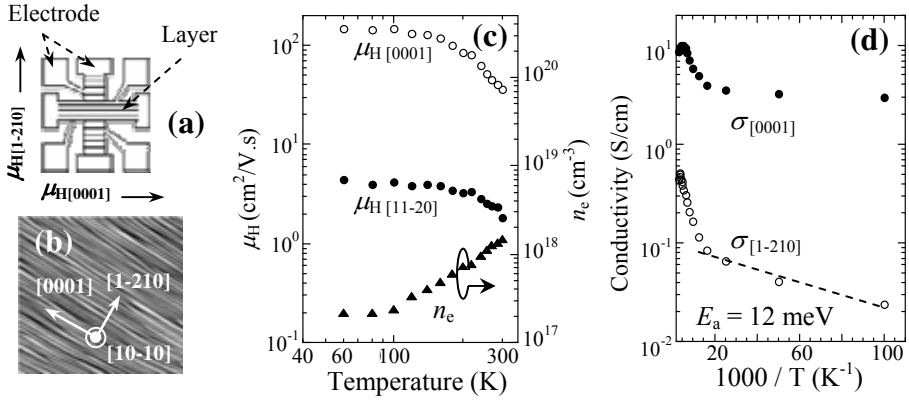

Fig. 17. (a) Hall bar patterned used to investigate anisotropic transport. (b) An AFM image of the $Mg_{0.12}Zn_{0.88}O$/ZnO MQWs. (c) Temperature dependence of $\mu_{H[0001]}$ and $\mu_{H[1-210]}$ for MQWs with a L_W of 2.8 nm. (d) Temperature dependence of $\sigma_{[0001]}$ and $\sigma_{[1-210]}$ for MQWs with a L_W of 2.8 nm.

Figure 18 (a) shows the ratio of $\mu_{H[0001]}$ and $\mu_{H[1-210]}$ as a function of temperature. The curves correpond to different L_W of 2.2, 2.8 and 4 nm. For MQWs with a L_W of 4 nm, we observed no anisotropic behavior. However, the anisotropy of the Hall mobiliyu increased to 52 for MQWs with a L_W of 2.8 nm at low temperatures. The transport properties indicate that an electron can move almost freely along the nanowires, but are blocked from moving perpendicular to the nanowires. We discuss a possible mechansim for this type of activation barrier. The large anisotropy of electron transport disappeared when a flat surface was realzied using Zn-polar MQWs, as shown in Fig. 18(b). Zn-polar MQWs shows an isotropic surface morphology and has sharp MgZnO/ZnO heterointerfaces, as confirmed using high-resolution X-TEM image [inset of Fig. 18(b)]. Interface-roughness scattering dominates low-temperature mobility in MQWs (Sakai et al., 1987). A slight roughness of the heterointerfaces induces a large fluctuation in quantization energy of confined electrons. This acts as a scattering potential barrier for electron motion and reduces mobility. Therefore, electrons may readily undergo frequent scattering in a direction perpendicular to the nanowires by potential barriers produced between nanowires, and, consequently, may become extremely immobile.

On the other hand, parallel conductance along the nanowires involves a lower scattering probality than perpendicular transport due to a weak heterointerface modulation. However, the P value for MQWs with a L_W of 2.2 nm decreased with a decrease in $\mu_{H[0001]}$. Inspection of polarized PL spectra showed that the energy fluctuations in the quantum well gradually increaed with decreasing L_W [Fig. 18]. A decreased Hall moblity with a narrowing of LW has been observed on very thin InAs/GaSb MQWs since energy fluctuations in a quantum well are caused by an increase in interface roughness (Tsujino et al., 2004; Szmulowicz et al., 2007). It is concluded, therefore, that the large transport anisotropy was obtained through both a quantum size effect and small energy fluctuations in the quantum well, i.e., when L_W was in the vicinity of 3 nm.

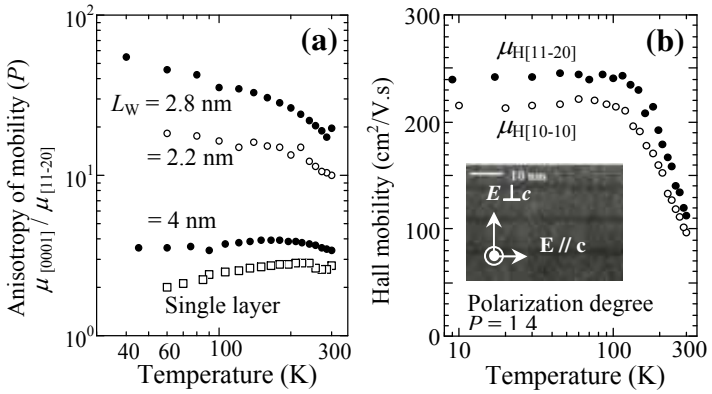

Fig. 18. (a) Temperature dependence of anisotropy of mobility (*P*) for M-nonpolar $Mg_{0.12}Zn_{0.88}O$/ZnO MQWs with different well thicknesses (L_W) of 2.2, 2.8 and 4 nm. (b) Temperature depednence of Hall mobiliy ($\mu_{H[11\text{-}20]}$) and ($\mu_{H[10\text{-}10]}$) for Zn-polar $Mg_{0.27}Zn_{0.73}O$/ZnO MQWs with a L_W of 2.4 nm.

Finally, the whole $\mu_{H[0001]}$ for MQWs was higher than that for *M*-nonpolar ZnO single layers as a result of the MQWs structure. However, it was lower than the mobility of ZnO single crystals, which is associated with thermal diffusions of extrinsic impurities from the hydrothermal ZnO substrates as a mobility-limited mechanism. Al atoms of the order of 1016 cm^{-3} were incorporated thermally into the samples from the substrates, as confirmed by secondary ion mass spectroscopy. It is noted that the presence of a background impurity results in a decrease of the whole Hall mobility for the MQWs.

6. Conclusion

We introduced a growth process for the anisotropic morphology that formed naturally on *M*-nonpolar ZnO (10-10) layer surfaces. Surface nanowires of high density elongated over 2 μm in length were observed during homoepitaxial growth. The surface nanowires gradually developed from elongated 3D mounds that originated from an ESB effect. Fabrication of *M*-nonpolar MQWs allowed examination of the relationship between electron transport and surface morphology. The observed transport anisotropy correlated strongly with the surface morphology, and was dependent on the crystal quality of the MQWs as determined by low-temperature polarized PL spectroscopy. The MQWs showed strong polarization light at 300 K with a *P* value of 0.43 for $E \perp c$. Polarization anisotropy was based on the selection rule and is attributed to emissions from *A*- and *C*-excitonic states. Deviation of the *P* value from unity at 10 K in MQWs was associated with the confinement-induced admixture of the P_z orbit to the *A*-excitonic states, being a characteristic of the *M*-plane quantum well. As a possible mechanism of the large conductance anisotropy, we proposed that electron motion perpendicular to the nanowire arrays was restricted by the potential barrier caused by an interface roughness between the surface nanowires.

In this chapter, we reported the formation of electrical channels with a 1-D conductance as in quantum wires using *M*-nonpolar MQWs on the lateral surface of a nanowires structrue. Semiconductor quantum wires have been the subject of extensive theoretical and experimental

studies over the past two to three decades. These are motivated by various unique quantum effects predicted in 1-D electronic systems, such as strong Coulomb correlation, suppression of electron scattering and an increase of quantum confinement. Q uantum wires have many potential applications to optoelectronic devices, such as high-mobility field-effect transistors. These surface nanowire structures contribute additional degrees of freedom for future studies of electron transport in field-effect transistors and magnetoelectric devices.

7. Acknowledgments

This work was supported in part by a Grant-in-Aid for Young Scientists (No. 18760231) from the Japan Society for the Promotion of Science, and a research grant from the Iketani Science and Technology Foundation (No. 081085-A)

8. References

Cassarin, M.; Maccato, M. & Vittadini, A. (1999). A comparative study of the NH_3 chemisorption on ZnO (10-10) and Cu_2O (111) nonpolar surfaces. *Chemical Physics Letters*, 300, 403-408.

Chen, Y.; Ko, H.-J.; Hong, S.-K.; Sekiuchi, T.; Yao, T. & Segawa, Y. (2000). Plasma-assisted molecular beam epitaxy for ZnO based II-V semiconductor oxides of their heterostructures. *J Vacuum Science & Technology B*, 18, 1514-1522.

Coli, G & Bajaj, K.K. (2001). Excitonic transitions in ZnO/MgZnO quantum well heterostructures. *Applied Physics Letters*, 78, 2861-2863.

Dulub, O.; Boatner, L.A. & Diebold, U. (2002). STM study of the geometric and electronic structure of ZnO (0001)-Zn, (000-1)-O, (10-10) and (11-20) surfaces, *Surface Science*, 519, 201-217.

Fan, W.J.; Xia, J.B.; Agus, P.A.; Tan, S.T.; Yu, S.F. & Sur, X.W. (2006). Band paramters and electronic structures of wurtzite ZnO and ZnO/MgZnO quantum wells. *Journal of Applied Physics*, 013702(1)-013702(4).

Fons, P.; Iwata, K.; Niki, S.; Yamada, A.; Matsubara, K. & Watanabe, M. (2000). Uniaxial locked growth of high-quality epitaxied ZnO films on (11-20) α-Al_2O_3. *Journal of Crystal Growth*, 209, 532-537.

Guha, S.; Madhukar, A. & Rajkumar, C. (1990). Onset of incoherency and defect introduction in the initial stages of molecular beam epitaxial growth of highly strained $In_xGa_{1-x}As$ on GaAs (100). *Applied Physics Letters*, 57, 2110-2112.

Hong, S.; Young, K. & Kahn, A. (1988). Structural studies od (331) GaAs surface. *Jounral of Vacuum Science & Technology A*, 7, 2039-2043.

Johnson, M.D.; Orme, C.; Hunt, W.; Graff, D.; Sudijono, J.; Sander, L.M. & Orr, B.G. (1994). Stable and unstable growth in molecular beam epitaxy. *Physical Review Letters*, 72, 116-119.

Kato, H.; Sano, M.; Miyamoto, K. & Yao. T. (2003). Effect of O/Zn flux ratio on crystalline quality of ZnO films grown by plasma-assisted molecular beam epitaxy. *Japanense Journal of Applied Physics*, 42, 2241-2244.

Kubo, M.; Oumi, Y.; Takaba, H.; Chatterjee, A.; Miyamoto, A.; Kawasaki, M.; Yoshimoto, M. & Koinuma, H. Homoepitaxial growth mechanism of ZnO (0001): Molecular-dynamics simulations. *Physical Review B*, 61, 16087-16092.

Maag, A.; Reimann, K. & Rübenacke, St. (1999). Band gaps, crystal-field splitting, spin-orbit coupling, and exciton binding energies in ZnO under hydrostatic pressure. *Solid State Communications*, 94, 251-254.

Makino, T.; Chia, C.H.; Tuan, N.T.; Sun, H.D.; Segawa, Y.; Kawasaki, M.; Ohtomo, A.; Tamura, K. & Koinuma, H. (2000). Room-temperature luminescence of wxcitons in ZnO/(Mg, Zn)O multiple quantum wells on lattice-matched substrates. *Applied Physics Letters*, 77, 4250-4252.

Mariano, A.M. & Hanneman, R.E. (1963). Crystallographic polarity of ZnO crystals. *Journal of Applied Physics*, 34, 384-388.

Matsui, H.; Saeki, H.; Kawai, T.; Sasaki, A.; Yoshimoto, M.; Tsubaki, M & Tabata, H. (2004). Characteristics of polarity-controlled ZnO films fabricated using the homoepitaxy technique. *Journal of Vacuum Science & Technology B*, 22, 2454-2461.

Matsui, H. & Tabata, H. (2005). Self-organized nanostripe arrays on ZnO (10-10) surfaces formed during laser molecular beam epitaxy growth. *Applied Physics Letters*, 87, 143109(1)-143109(3).

Matsui, H.; Tabata, H.; Hasuike, N.; Harima, H. & Mizobuchi, B. (2005). Epitaxial growth and characteristics of N-doped anatase TiO_2 films grown using a free-radical nitorgen oxide source. *Journal of Applied Physics*, 97, 123511(1)-123511(8).

Matsui, H. & Tabata, H. (2006). Correlation of self-organized surface nanostructures and anisotropic electron transport in nonpolar ZnO (10-10) homoepitaxy. *Journal of Applied Physics*, 99, 124307 (1) – 124307 (8).

Matsui, H.; Hasuike, N.; Harima, H. & Tabata, H. (2006). Critical thickness and lattice relaxation of Mg-rich strained $Mg_{0.37}Zn_{0.63}O$ (0001) layers towards multiple-quantum wells. *Journal of Applied Physics*, 99, 024902(1)-024902(7).

Matsui, H.; Hasuike, N.; Harima, H.; Tanaka, T. & Tabata, H. (2006). Stranski-Krastanov growth in $Mg_{0.37}Zn_{0.63}O$/ZnO heteroepitaxy: Self-organized nanodots and local composition separation. *Applied Physics Letters*, 89, 091909(1)-091909(3).

Matsui, H.; Hasuike, N.; Harima, H. & Tabata, H. (2008). Growth evolution of surface nanowires and large anisotropy of conductivity on MgZnO/ZnO quantum wells based on *M*-nonpolar (10-10) ZnO. *Junral of Applied Physics*, 104, 094309(1)-094309(6).

Matsui, H. & Tabata, H. (2009). In-plane anisotropy of polarized photoluminescence in *M*-plane (10-10) ZnO and MgZnO/ZnO multiple quantum wells. *Applied Physics Letters*, 94, 161907(1)-161907(3).

Michely, T. & Krug, J. (2004). Patterns and processes in crystal growth far from equilibrium. *Islands, Mounds, Atoms*. Springer Series in Surface Sicence 42, 1-305. (Springer, New York).

Niwa, A.; Ohtoshi, T. & Kuroda, T. (1996). Tight-binding analysis of the optical matrix element in wurtzite- and zincblende- GaN quantum wells. *Japanense Junral of Applied Physics*, 35, L599-L601.

Ohno, Y.; Higashiwaki, H.; Shimomura, S. & Hiyamizu, S. (2000). Laser operation at room temperature of self-organized $In_{0.1}Ga_{0.9}As/(GaAs)_6(AlAs)_1$ quantum wires grown on (775) B-oriented GaAS substrates by molecular beam epitaxy. *Journal of Vacuum Science & Tecnology B*, 18, 1672-1674.

Ohtake, A.; Miwa, S.; Kuo, L.H.; Kinura, K.; Yasuda, T.; Jin, C. & Yao, T. Polar surface dependence of epitaxy processes: ZnSe on GaAs {111}A, B-(2 x 2). *Applied Surface Science*, 130-132, 398-402.

Ohtomo, A.; Kawasaki, M.; Koida, T.; Masubuchi, K.; Koinuma, H.; Sakurai, Y.; Yoshida, Y.; Yasuda, T. & Segawa, Y. (1998). $Mg_xZn_{1-x}O$ as II-IV wide gap semicondcutor alloy. *Applied Physics Letter*s, 72, 2466-2468.

Parker, T.M.; Condon, N.G.; Lindsay, R.; Leibsle, F.M. & Thornton, G. (1998). Imaging the polar (000-1) and nonpolar (10-10) surfaces of ZnO with STEM. *Surface Science*, 415, L1046-L1050.

Reynolds, D.C.; Look, D.C.; Jogai, B.; Litton, C.W.; Cantwell, G. & Harsch, W.C. (1999). Valence band ordering in ZnO. *Physcial Review B*, 60, 2340-2344.

Reynolds, D.C.; Look. D.C.; Jogai, B.; Litton, C.W.; Collins, T.C.; Harris, T.; Callahan, M.J.; Bailey, J.S. (1999). Strain splitting of the Γ_5 anf Γ_6 free excitons in ZnO. *Journal of Applied Physics*, 86, 5598-5600.

Sakai, H.; Noda, T.; Hirakawa, K.; Tanaka, M. & Matsusue, T. (1987). Interface roughnes scattering in GaAs/AlAs quantum wells. *Applied Physics Letters*, 51, 1934-1936.

Schönher, H.P.; Fricke, J.; Niu, Z.; Friedland, K.J.; Nötzel, R. & Ploog, K.H. (2001). Uniform multiatomic step arrays formed by atomic hidrogen assisted molecular beam epitaxy on GaAs (331) substrates. *Applied Physics Letters*, 72, 566-568.

Schwoebel, R.L. (1966). Step motion on crystal surfaces. *Journal of Applied Physics*, 37, 3862-3686.

Sumiya, M.; Yoshimoto, K.; Ito, T.; Ohtsuka, K.; Fuke, S.; Mizuno, K.; Yoshimoto, M.; Koinuma, H.; Ohtomo, A. & Kawasaki, M. (2000). Growth mode and surface morphology of a GaN film deposited along the N-face polar direction on c-plane sapphire substrate. *Jounral of Applied Physics*, 88, 1158-1165.

Szmulowicz, F.; Elhanri, S.; Haugan, H.J.; Brown, G.J. & Mitchel, W.C. (2007). Demonstration of interface-scattering-limitted electron mobilities in InAs/GaSb superlattices. *Journal of Applied Physics*, 043706(1)-043706(5).

Thomas, D.G. (1960). The exciton spectrum of zinc oxide. *Journal of Physical & Chemcial Solids*, 15, 86-89.

Tsujino, S.; Falub, C.N.; Müller, E.; Scheinert, M.; Drehl, L.; Gennser, D.; Fromherz, T.; Borak, A.; Sigg, H.; Grützmacher, D.; Campidelli, Y.; Kermarrec, O. & Bensahel, D. (2004). Hall mobility of narrow $Si_{0.2}Ge_{0.8}$-Si quantum wells on $Si_{0.5}Ge_{0.5}$ relaxed buffer substrates. *Applied Physics Letters*, 84, 2829-2831.

Tsukazaki, A.; Ohtomo, A.; Kita, T.; Ohno, Y.; Ohno, H. & Kawasaki, M. Quantum Hall effect in polar oxide heterostructures. *Science*, 78, 2861-2863.

Sharma, A.K.; Narayan, J.; Muth, J.F.; Teng, C.W.; Jin, C.; Krit, A.; Kobas, R.M. & Holland, O.W. (1999). Optical and structural properties of epitaxial $Mg_xZn_{1-x}O$ alloys. *Applied Physics Letters*, 75, 3327-3329.

Viguè, F.; Vennégnès, P.; Vèzian, S.; Laùgt, M. &Fourie, J.-P. (2001). Defect characterization in ZnO layers grown by plasma-enhanced molecular beam epitaxy on (0001) sapphire substrates. *Applied Physics Letters*, 79, 194-196.

Vipute, R.D.; Talyansky, V.; Tranjanovic, Z.; Choopun, S.; Downes, M.; Sharma, R.P.; Venkatesan, T.; Wood, M.C.; Lareau, R.T.; Jones, K.A. & Ilidais, A.A. (1997). High quality crystalline ZnO buffer layers on sapphire (0001) by pulse laser deposition for III-V nitrides. *Applied Physics Letters*, 70, 12735-12737.

Waag, A.; Schmeusser, S.; Bicknell-Tassius, R.N.; Yakovlev, D.R.; Ossau, W.; Landwehr, G.; Uraltsev, I.N. (1991). Molecular beam epitaxial growth of ultra-thin CdTe-CdMnTe quantum wells and their characterization. *Applied Physics Letters*, 59, 2995-2997.

Wang, K.L. & Voliotis, V. (2006). Epitaxial growth and optical properties of semiconductor quantum wires. *Journal of Applied Physics*, 99, 121301(1)-121302(38).

Yan, F.W.; Zhang, W.J.; Zhang, R.G.; Cui, L.Q.; Liang, C.G. & Liu, S.Y. (2001). Formation and characterization of (553) *B* $In_{0.15}Ga_{0.85}As$/GaAs quantum wire structure. *Journal of Applied Physics*, 90, 1403-1406.

Yu, P.; Tang, Z.K.; Wong, G.K.L.; Kawasaki, M.; Ohtomo, A.; Koinima, H. & Segawa, Y. (1997). Ultraviolet spontaneous and stimulated emissions from ZnO microcrystalline thin films at room temperature. *Solid State Communications*, 103, 459-464.

Yu, Y.M. & Liu, B.G. (2008). Contrasting morphologies of O-rich ZnO epitaxy on Zn- and O-polar thin film surfaces: Phase-field model. *Physical Review B*, 195327(1)-195327(6).

Nanowires

Edited by Paola Prete

ISBN 978-953-7619-79-4
Hard cover, 414 pages
Publisher InTech
Published online 01, February, 2010
Published in print edition February, 2010

This volume is intended to orient the reader in the fast developing field of semiconductor nanowires, by providing a series of self-contained monographs focusing on various nanowire-related topics. Each monograph serves as a short review of previous results in the literature and description of methods used in the field, as well as a summary of the authors recent achievements on the subject. Each report provides a brief sketch of the historical background behind, the physical and/or chemical principles underlying a specific nanowire fabrication/characterization technique, or the experimental/theoretical methods used to study a given nanowire property or device. Despite the diverse topics covered, the volume does appear as a unit. The writing is generally clear and precise, and the numerous illustrations provide an easier understanding of the phenomena described. The volume contains 20 Chapters covering altogether many (although not all) semiconductors of technological interest, starting with the IV-IV group compounds (SiC and SiGe), carrying on with the binary and ternary compounds of the III-V (GaAs, AlGaAs, GaSb, InAs, GaP, InP, and GaN) and II-VI (HgTe, HgCdTe) families, the metal oxides (CuO, ZnO, ZnCoO, tungsten oxide, and PbTiO3), and finishing with Bi (a semimetal).

InTech Europe
University Campus STeP Ri
Slavka Krautzeka 83/A
51000 Rijeka, Croatia
Phone: +385 (51) 770 447
Fax: +385 (51) 686 166
www.intechopen.com

InTech China
Unit 405, Office Block, Hotel Equatorial Shanghai
No.65, Yan An Road (West), Shanghai, 200040, China
中国上海市延安西路65号上海国际贵都大饭店办公楼405单元
Phone: +86-21-62489820
Fax: +86-21-62489821